Accepted Manuscript

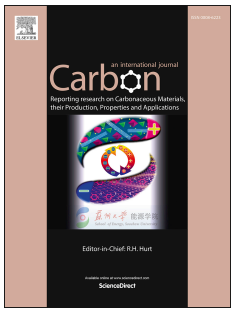

Synthesis of carbon nano-onions doped with nitrogen using spray pyrolisis

E. Tovar-Martinez, J.A. Moreno-Torres, J.V. Cabrera-Salazar, M. Reyes-Reyes, Luis F. Chazaro-Ruiz, R. López-Sandoval

PII: S0008-6223(18)30790-5

DOI: 10.1016/j.carbon.2018.08.056

Reference: CARBON 13411

To appear in: *Carbon*

Received Date: 12 June 2018

Revised Date: 21 August 2018

Accepted Date: 27 August 2018

Please cite this article as: E. Tovar-Martinez, J.A. Moreno-Torres, J.V. Cabrera-Salazar, M. Reyes-Reyes, L.F. Chazaro-Ruiz, R. López-Sandoval, Synthesis of carbon nano-onions doped with nitrogen using spray pyrolisis, *Carbon* (2018), doi: 10.1016/j.carbon.2018.08.056.

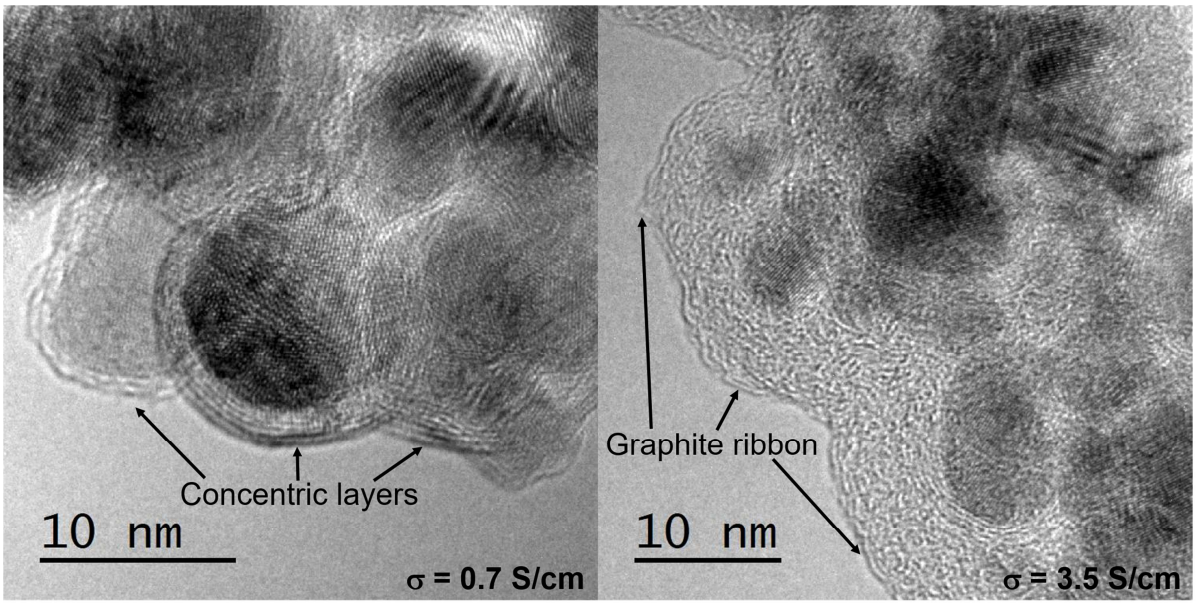

Synthesis of carbon nano-onions doped with nitrogen using spray pyrolisis

E. Tovar-Martinez[1,2], J. A. Moreno-Torres[2], J. V. Cabrera-Salazar[1], M. Reyes-Reyes[2] , Luis F. Chazaro-Ruiz[3] and R. López-Sandoval[1*]

[1] Advanced Materials Department, IPICYT, Camino a la Presa San José 2055, Col. Lomas 4a sección, San Luis Potosí 78216, Mexico.

[2] Instituto de Investigación en Comunicación Óptica, Universidad Autónoma de San Luis Potosí, Álvaro Obregón 64, San Luis Potosí 78000, Mexico.

[3] Enviromental Science Department, IPICYT, Camino a la Presa San José 2055, Col. Lomas 4a sección, San Luis Potosí 78216, Mexico.

Abstract

In this work, we have synthesized carbon nano-onions (CNOs) doped with nitrogen and iron carbide core. These nanostructures were synthesized pyrolysing various alcohol-benzylamine reaction mixtures. These CNOs showed a certain degree of functionalization of their surfaces, depending of the solvent, as well as *n*-type doping due to the inclusion of N atoms in the graphene layers. Ratios of O atoms to C atoms as well as to N atoms of the pyrolyzed solution play an important role in the morphology of the CNOs and on the phase of the iron core. Differences in the morphology of the samples have an important effect on their electrical conductivity as well as in their electrochemical properties. Synthesized samples showing well-defined CNOs, the sintering between them is negligible, have a low conductivity and higher capacitance, while those samples showing the best conductivities and lower capacitances, the CNOs in samples are connected between them by turbostratic graphite ribbons, in similar way to the CNOs synthesized from carbon nanodiamond annealed in argon atmosphere.

*Corresponding author. E-mail: sandov@ipicyt.edu.mx (Román López-Sandoval)

1. Introduction

Nanoparticles can be protected from degradation due to environmental conditions, at the same time that their intrinsic properties are preserved when they are encapsulated. Some of the structures that encapsulate are carbon nanotubes or carbon layers [1,2]. The encapsulation of nanoparticles has attracted the attention for its promising applications, such as in information technology and biomedicine [3-6]. In some technological applications, such as in gas sensors, it is possible to use hollow carbon nanoparticles instead of carbon layers encapsulating nanoparticles [7-8]. In other cases, these carbon nanoparticles are quasi-spherical and consist only of concentric graphene layers [9-11]. In general, these kind of carbon are indistinctly called carbon nano-onions (CNOs) [11]. CNOs were discovered by S. Iijima in 1980 [9], but it was D. Ugarte who reported a reproducible technique for obtaining these nanostructures by irradiation of carbon soot with an electron beam [10]. Several techniques have been used for the synthesis of this material [11]. However, the most widely used method is the graphitization of carbon nanodiamonds at high temperatures (1100-1700 °C) in an inert gas or under vacuum conditions [11-14]. Other techniques to synthesize CNOs include laser excitation, ion implantation and chemical vapor deposition (CVD) [15-20].

CNOs have good electrical characteristics for their use in electrical double layer capacitors (EDLC) because they can be synthesized with small diameters <10 nm [21-24], which make them suitable for their use in EDLC. This is related to the fact that the smaller the CNOs diameters, the larger the exposed surface area and, thus, much larger the capacitance [11, 21-24]. However, the use of CNOs in EDLC, as well as in other possible technological applications, requires their surface functionalization [25-27] and, in some cases, the modification of their electronic properties [28-30]. In general, the surface functionalization of CNOs is carried out by chemical oxidation either with inorganic acids [31,32] or with potassium hydroxide [33]. This chemical activation generates surface oxygenated functional groups, which increase the solubility of the CNOs in polar solvents. However, this surface functionalization generates defects and, as a consequence, a loss of the sp^2 character of the graphene layer, with a consequent loss of its great electrical conductivity. To retain the high conductivity of CNOs, it is necessary to perform a surface functionalization using mild conditions, such as diluted nitric acid [31,34]. On the other

hand, the electronic properties of CNOs can be modified introducing heteroatoms in the graphene lattice [35-39]. This method is effective to modify the physical and chemical properties of CNOs, resulting in a promising approach for their use in various applications. The incorporation of N atoms in the graphene layer generates an excess of electrons in the carbon nanostructures [28], which are called *n*-type nanostructures. Furthermore, CNOs doped with N present high catalytic activity in electron transfer reactions [37-39].

In this paper, we report the synthesis of CNOs doped with N atoms, which encapsulate iron carbide nanoparticles. These materials were synthesized using spray pyrolisis at 850 °C of several reaction mixtures. The reaction mixtures contained ethanol (with C/O = 2 atom ratio) or isopropanol (with C/O = 3 atom ratio), as the main sources of carbon, benzylamine, as the agent containing the nitrogen dopant, and ferrocene as a catalyst. Two alcohol to benzylamine volume ratios were used in order to vary the quantities of C, O and N atoms in the reaction mixture. This allowed to observe the effect of different C/O and O/N ratios in the crystal arrangement of the graphene layers surrounding the metal nanoparticles, the phase of the synthesized iron nanoparticle, the amount of N heteroatom introduced in the graphene lattice, with the consequent change in their physical and chemical properties, and the anchoring of oxygenated functional groups on the surfaces of the nanostructures. This method of synthesis of CNOs is a low cost process and good controlled, since it allows the obtaining of pure CNOs, that is without the presence of other carbon nanostructures such as nanotubes, nanofibers, among others in the final yield.

2. Experimental section

2.1 Synthesis of CNOs

Reaction mixtures were prepared using ethanol or isopropanol, as main sources of carbon and, benzylamine, as a reactive containing the nitrogen dopant. The relationships volume to volume (v/v) were 9 to 1 (91) and 4 to 1 (41) (alcohol to benzylamine), which correspond to 16.8:1 molar ratios (C/O=2.4 and O/N=16.8 atom ratios) and 7.5:1 (C/O=2.9 and O/N=7.5 atom ratios) for ethanol to benzylamine (EB) mixtures and 12.9:1 (C/O=3.6 and O/N=12.9 atom ratios) and 5.7:1 (C/O=4.2 and O/N=5.7 atom ratios) for isopropanol to benzylamine (IB) mixtures. In general, volume ratios were used instead of molar ratios. In all experiments, the total volume of the solutions was set at 11 mL to which 3 wt% of

ferrocene was added. The reaction mixture was ultrasonicated during 20 minutes. The final homogeneous solution was transferred to a container to produce a spray that was thermolized at 850 °C using a tubular furnace and Ar as the gas carrier (0.20 L/min). Subsequently, the tubular furnace was cooled down to room temperature and the material was obtained by scraping the quartz tube**.**

2.2 Characterization of CNOs

Samples for conventional and high-resolution transmission electron microscopy (TEM, HRTEM) were prepared by dissolving the powder in isopropanol using an ultrasound bath for 20 minutes. A solution drop was put on lacey-carbon grid and the isopropanol was allowed to evaporate. Grids were examined using a TECNAI-F30 HRTEM microscope operated at 300 kV. Raman spectra were recorded at room temperature using an InVía Micro-Raman Renishaw system. The 514.5 nm (2.51 eV) laser excitation line was focused using the 50× magnification objective to a ~ 1μm spot. The X-ray diffraction analysis was performed using a SmartLab RIGAKU diffractometer, which has a copper tube as an X-ray generator and a NaI scintillation detector. The XRD measurements were obtained at room temperature with a step of 0.01° in a range of 35 to 70°. XPS measurements were performed with the PHI5000 VersaProbe II using a monochromatic Al-Ka X-ray beam.

2.3 Electrode preparation and electrochemical measurements

The working electrode (WE) was prepared using the following procedure: (1) a binder agent, poly(vinylidene fluoride) (PVDF), was dissolved in 5 mL of N,N-dimethylformamide (DMF); (2) activated carbon derived from coconut shells (AC-CS), as well as synthesized CNOs, used as conductive additive and active material respectively, were added to the PVDF dissolution. The weight ratios (wt%) were 22.13/67.87/10 of PVDF, AC-CS and CNOs respectively. This mixture was stirred at 100 ºC, allowing the complete solvent evaporation to obtain a paste, which was deposited on a predetermined active area of a glassy carbon electrode used as current collector. Finally, the electrode was set to dry at 80 ºC. The mass loading of the electrodes ranged from 5 to 10 mg cm^2 which is a standard loading for evaluating the properties of an electrode for capacitors. The electrochemical measurements were carried out in an electrochemical cell with a three

electrode arrangement containing 2M KOH aqueous solutions using a VMP3 Bio-Logic SAS potentiostat/galvanostat controlled by EC-Lab software. The Hg/HgO/NaOH 1M system was used as a reference electrode and a platinum gauze as a counter electrode. The prepared electrodes were tested by cyclic voltammetry (CV) performed at different scan rates ranging from 1 to 5 mVs^{-1} in a potential window from -0.1 to 0.2 V. The specific capacitances were calculated from the CV curves by the following equation [33]:

$C = \int i\, dV/(m\upsilon\Delta V)$ (1)

where i is the response current, m is the mass of the CNOs, ΔV is the potential window, υ is the scan rate.

3. Results and Discussion

The synthesized materials were black powders that showed ferromagnetic properties. TEM micrographs (Fig. 1) revealed that the nanoparticles present quasi-spherical shape and have a core-shell structure, with an iron core and carbon shells. The CNOs diameters varied in the range of 5-14 nm, with the exception of EB-41 sample, which show a mix between small (<14 nm) and large CNOs (> 30 nm) (Fig. 1b). The synthesized nanoparticles have, in general, diameters < 15 nm, regardless of the alcohol used and the volume proportions of alcohol to benzylamine. The HRTEM micrographs show that the carbon layers are firmly surrounding the central nanoparticles (Figs. 2 and 3), and no gaps are observed between the iron core and the carbon shells. The interplanar distance between the graphene sheets is approximately 0.35 nm (Figs. 2 and 3), which is close to that of the (002) planes of the graphite indicating a good graphitization. Even more, the micrograph of sample EB-91 (Fig 2a-b) shows well graphitized CNOs, which can be distinguished individually, while the carbon nanostructures of EB-41 (Fig. 2c-d and Fig. S1 in Supplementary information), IB-91 (Fig 3a-b and Fig. S2 in Supplementary information) IB-41 (Figs 3c-d and Fig. S3 in Supplementary information) samples are more similar to iron nanoparticles embedded in carbon nanosheets. These morphological differences, as will be shown below, have important consequences on the conductive and electrochemical properties of CNOs films. From these results, we can notice that the C/O ratio used in the reaction mixture is an important parameter that influences the differences observed in the synthesized CNOs. Also, it is possible to observe that the iron cores of these CNOs are crystalline and show an

interplanar distance of 0.20 nm (Figs. 2 and 3), which can be related to the (110) planes of the Fe-bcc (JCPDS 6-0696) or to the (031) planes of the Fe_3C crystal (JCPDS 35-0775). Additional identification of the iron phase was carried out with X-ray diffraction measurements (XRD), whose XRD patterns are shown in Figure 4. XRD patterns indicate the presence of iron carbide (Fe_3C, cohenite) in all synthesized samples. No characteristic peaks of iron oxide, such as magnetite or hematite, were observed, as previously reported by our group using alcohol mixtures [20]. This result is important since it indicates that the reaction mixture defines the type of iron core produced in the synthesized nanoparticles. On the other hand, the graphite peak (002) is very weak and wide in the XRD patterns, which shows that the carbon structures are partially graphitized and the samples consist mainly of iron carbide cores covered by a few layers of turbostratic graphite.

Another technique used for the characterization of synthesized CNOs was Raman spectroscopy. Fig. 5 shows the Raman spectra using a 514.5 nm laser line (2.41 eV) and at low laser power (0.5 mW), to avoid the erosion of the carbon shells protecting the iron cores of the synthesized samples. From figure, two Raman bands are observed: one at ~1330 cm^{-1} (band D1) and the other at ~1595 cm^{-1} (band G). It was shown by Tuinstra and Koenig that the ratio of the maximum intensity of the band D (I_D) to the maximum intensity of the G band (I_G) is inversely proportional to the in-plane crystal size L_a, that is $I_D/I_G \propto 1/L_a$ [40]. This relationship is widely used to characterize the quantity and type of defects in graphitic materials [40, 41]. Tuinstra and Koening obtained this result studying the relationship between I_D/I_G ratios, using Raman spectroscopy, and the crystallite size of the graphene plane, using X-ray diffraction. Based on these ideas, Knight and White carried out a series of measurements and observed that the size of the graphite nanocrystals can be calculated using Raman spectra with the help of the following equation [40,41]:

$$L_a\,(nm) = C_\lambda\,(I_D/I_G)^{-1} \quad (2),$$

since $C_{\lambda=512nm}$ = 4.4 nm. This equation has been popularly applied to obtain results comparable to those obtained by X-ray diffraction. However, this equation is only valid when the Raman measurement is performed using a 514.5 nm laser line. A new equation for the calculation of crystal sizes was proposed by Cançado et al. [42], in which the

quotient of the integrated intensities of both Raman bands (A_D/A_G) is used for the calculation of the crystallites sizes for any excitation wavelength

$$L_a\ (nm) = (560/ E_l^4)\ (A_D/A_G)^{-1} \quad (3),$$

where E_l is the laser excitation energy used in the Raman measurement in eV units. However, for using these equations adequately, a good definition of the D1 band and the G band is necessary, which only occurs in single crystal or in polycrystalline graphite [40,42]. In the case of CNOs, as well as in other carbon nanostructures, other bands related with the disorder should be considered [43-46]: one at ~ 1180 cm^{-1} (D4), assigned to sp^3 carbon or to impurities, another at ~1500 cm^{-1} (D3), associated to the amorphous carbon, and another one at ~1620 cm^{-1} (D2), which has been related to the graphene layers at the surface of the graphite nanocrystals. Then, to obtain a good determination of the L_a sizes is required to consider the presence of these bands by an adequate deconvolution of the Raman spectra obtained from the synthesized nanostructures. For this reason, the Raman spectra were fitted using 4 Lorentzian and one Gaussian curves, which are shown in Fig. 5. From figure and curve fittings (Table I), we observe that the contributions of D2 band to the Raman spectra are negligible and it is not necessary to consider its contribution. From both equations the values of crystallite sizes L_a for the various synthesized CNOs using the different reaction mixtures are listed in Table II. From these results, it is possible to observe that depending on the formulas used to calculate the crystallite sizes, different L_a values are obtained for the same reaction mixture, and there is not a direct correlation between the C/O and O/N ratios of the different reaction mixtures with the size of the graphene crystallites. Additionally, from Table II we can note that the synthesized samples using the same alcohol to benzylamine reaction mixture, but with different volume ratios, have the same L_a tendency regardless of the formula used for their calculation.

In the Raman spectra obtained using low laser power (Fig. 5), there were not bands associated to iron carbide nanoparticles, which should be in the region between 200 and 700 cm^{-1}, similar to iron oxides nanoparticles [47-49]. This could be due to the Raman inactive vibrational modes of the single crystal of iron carbide [50]. However, some studies show the existence of Raman bands from iron carbide nanostructures [51], although

without mentioning the laser power used for their characterization. It is likely that iron carbide is a poor Raman scatterer, and then a high laser power is required for observing its Raman bands. For this reason, the laser power was increased to 2.5 mW for performing Raman spectroscopy of the synthesized samples. Additionally, with a high laser power, it is possible to study the thermal stability of the iron phase encapsulated by the layers of turbostratic graphite [49]. In Figure 6, Raman spectra of the different synthesized samples are observed. These Raman spectra show several bands: at 222 cm^{-1}, 241 cm^{-1}, 288 cm^{-1}, 302 cm^{-1}, 405 cm^{-1}, 495 cm^{-1} and 604 cm^{-1}, which correspond to hematite (α-Fe_2O_3) [42]. At his laser power, Raman bands corresponding to the graphitic layers decrease in intensity and show an increase in the intensity of the D band with respect to the G band, indicating the amorphization of the graphitic layers as well as their erosion. This implies that the use of high power laser first removes the turbostratic graphite layers surrounding the iron carbide nanoparticles and, then, the iron carbide particles are laser heated at high temperatures, react with oxygen and change its phase to hematite. A similar effect is observed when these structures are heated up at 500 °C in room conditions. These results suggest that the vibrational modes of the iron carbide nanoparticles are Raman inactive and the Raman bands reported in the literature for these nanoparticles are phase transformations due to the high power used during their Raman characterization [50,51].

One of the most interesting properties of CNOs is their good electrical conductivity, which make them attractive for applications in high-power EDLC capacitors or for their use as an additives in EDLC capacitors based on activated carbon particles, where only small amounts are used (~ 5-10% mass %) [21-24]. We have carried out electrical conductivity (σ) measurements of the synthesized samples using the four-point method in pellets fabricated using a mechanical press, obtaining the following results: σ = 0.7 S/cm (EB-91), σ = 2.2 S/cm (EB-41), σ = 3.5 S/cm (IB-91) and σ = 2.2 S/cm (IB-41). Additionally, we have used other film fabrication technique. Quartz substrates were introduced in the synthesis device and CNOs were directly deposited on these substrates. The conductivities of the films showed similar conductivities to those obtained for pellets fabricated with the same type of sample. We observe that the conductivity of the samples depends on the reaction mixture, obtaining the best results for samples where the C/O ratio is larger and O/N ratio is smaller. In addition, the highest conductivity value, 3.5 S/cm, of

IB-91film is comparable to the values reported by McDonough et al. (~ 4 S/cm) [52] and is an order of magnitude higher than activated carbon (<0.5 S/cm) [53]. However, from Table II, we cannot assume that the CNOs films with greater electrical conductivity present larger L_a sizes. Even more, in the case of reaction mixtures with the same alcohol but different volume ratios, the samples presenting larger L_a values (Table II) are those whose films show a lower σ. This result indicates that other parameters play a key role in the conductivity. One of them is the amount of amorphous carbon on the CNOs surface [45,46]. It has been considered that the I_{D4}/I_G ratio provides information on the relative amount of amorphous carbon in the sample [45]. The I_{D4}/I_G values of the synthesized samples correspond to 0.23, 0.16, 0.20, 0.16, for EB-91, EB-41, IB-91, IB-41 samples, respectively. Then, from these results, the EB-91 sample, despite having a larger L_a value, contains more amorphous carbon on its surface, which is in part responsible for its lower σ. In addition, the value σ in Table II is inversely proportional to D4/Dtot, i.e. to the contribution of the amorphous carbon to the total area of D band. On the other hand, it has been shown that the synthesized CNOs from carbon nanodiamonds annealed in flowing argon show larger agglomerate sizes compared to those synthesized using vacuum annealing of carbon nanodiamond [46]. This increase in the agglomeration of argon flowing CNOs comes from particle sintering and redistribution of carbon during the thermal annealing. Fabricated films using CNOs annealed in flowing argon present better conductivities than fabricated films with vacuum annealing CNOs. The differences in conductivities between both kinds of samples are due to the presence of graphitic ribbons between argon annealing CNOs. From HRTEM micrographs (Figs. 2, 3 and Figs. S1-S3 in Supplementary information) of IB-91, EB-41 and IB-41 samples, which present the best conductivities, we observe that they are similar to graphite nanosheets with embedded iron carbide nanoparticles. If these nanostructures are studied in a detailed manner, it is observed that the CNOs in these samples are connected between them with turbostratic graphite ribbons, in a similar way to the argon annealing CNOs. This explains that even though the EB-91 sample is well graphitized compared with the others, these present lower conductivities.

Other important parameter for modifying the physical, chemical and electric properties of CNOs is the amount of N atoms in the graphene lattice as well as the chemical

environment surrounding them, where N atoms act as an electron donor. Survey and high-resolution XPS measurements of the CNOs samples were carried out at two different points of the samples using a 100 μm X-ray beam size, allowing to corroborate the sample homogeneity. In the case of EB-91, IB-91, IB-41 samples, these showed similar atomic percentages of C, O, N, Fe at both measured points while those synthesized using EB-41 reaction mixture showed atomic percentages of O, N, Fe different in the measured points (Table S1 in Supplementary information). These results are in good agreement with the TEM micrographs. TEM micrographs of EB-41 sample show that this is composed of a mixture of nanostructures with two different sizes of the iron carbide core, some with sizes less than 14 nm and others with sizes larger than 30 nm. In contrast, EB-91, IB-91, IB-41 samples present a good homogeneity in the nanostructure sizes. High-resolution XPS measurements of C1s state of the four synthesized samples are shown in Fig. 7. From figure, it is observed that the C1s spectra show a peak at approximately 284.4 eV, with a tail at a higher binding energy. A detailed analysis of the data coming from the high-resolution XPS spectra leads to the following attributions of the observed components (Table S2 in Supplementary information). The peak at 283.5 eV is assigned to the contributions of the C-Fe bonds [54,55]. The existence of this peak corroborates the presence of the iron carbide phase in the synthesized samples. In addition, the carbon layers encapsulating these metal nanoparticles show thicknesses less than 10 nm, where XPS is a superficial technique able to measure the chemical states of atoms that are between 0 to 10 nm of sample surface. A second peak related to graphitic carbon is observed at 284.4 eV, indicating that carbon layers are encapsulating metal nanoparticles [54-57]. In addition, a carbon atom contribution with a sp^3 hybridization is found at 285.3 eV [55-57]. From the Table S2, it is observed that the EB-91 and IB-91 samples show a greater ratio of the sp^3 contribution to the C1s spectrum while EB-41 and IB-41 samples show a smaller sp^3 contribution, which is in good agreement with Raman measurements. C1s spectra also show the presence of 3 additional peaks, which are due to carbon-oxygen interactions and are found at 286.7, 288.3 and 289.2 eV, corresponding to hydroxyl, carbonyl and carboxyl groups [56-58], respectively. The presence of the oxygenated functional groups comes from the use of alcohols in the reaction mixture, indicating that the CNOs present a certain degree of surface functionalization, which allows a good

dissolution of CNOs in polar solvents (Fig. S4 in Supplementary information). Using high-resolution XPS measurements of O1s spectra of the synthesized samples, the presence of oxygenated functional groups was corroborated (Fig. S5 and Table S3 in Supplementary information). Additionally, EB-41 and IB-41 samples show a small contribution of a metal oxide, which was undetectable using X-rays, i.e. iron carbide cores contain a thin layer of iron oxide. The presence of N atoms acting as a dopant within the graphene lattice is also observed in these C1s spectra, which may be related to the use of benzylamine as a precursor of the synthesized samples. The effect of N atoms in C1s spectra can be observed as two additional peaks at 286.1 and 287.3 eV, related to their sp^2 and sp^3 hybridization, respectively [56, 59]. Moreover, the XPS survey measurements show the following relationship IB-41> EB-41> EB-91> IB-91 in N average atomic concentration. From these results, we observe that although N atoms can act as electron donors of the graphene lattice, N doping cannot be responsible for the greater conductivity of IB-91 sample. High-resolution XPS measurements of N1s spectra (Fig. 8 and Table S4 in Supplementary information) show the presence of nitrogen atoms in different chemical environments. The N1s spectra were deconvoluted in 4 peaks. The peaks are located at 398.6 eV, at 400.0 eV, at 401.1 eV and at 403.4 eV, which correspond to pyridinic nitrogen, pyrrolic nitrogen, graphitic nitrogen and pyridine-N-oxide groups, according to the reported in the literature [54, 56, 59-62].

Cyclic voltammetry was carried out with electrodes fabricated with representative samples of the two morphologies of the synthesized CNOs, EB-91 and IB-91, which correspond to the one with the lowest conductivity and the highest conductivity respectively. The CVs of the EB-91 and IB-91 electrodes (Figs. 9a and 9b, respectively) presented the characteristic rectangular shape of a capacitive behavior. At a scan rate of 1 mVs^{-1}, the electrode with the EB-91 sample presented the largest specific capacitance C = 101.8 Fg^{-1}, while the lowest specific capacitance corresponded to the electrode with IB-91 sample, which was C=24.9 Fg^{-1}. It is important to mention that the voltammogram of the conductive additive was flat. These differences in specific capacitances are related to sample morphology, since the CNOs of EB-91 sample were observed as individual particles, thus, the surface area of each of them contributes to the capacitance. On the other hand, the IB-91 samples were observed as carbon nanosheets with embedded iron carbide

nanoparticles, therefore, the access of the ions to the surface of CNOs is hindered. These results highlight the importance of increasing the conductivity of the CNOs, but without affecting their effective surface area for their use in EDLC devices.

4. Conclusions

In this work, CNOs doped with nitrogen encapsulating iron carbides nanoparticles were synthesized using several alcohol-benzylamine mixtures. Two kinds of alcohols, ethanol (C/O = 2 atom ratio) and isopropanol (C/O = 3 atom ratio), were used as the main source of carbon, benzylamine mainly as the source of nitrogen and ferrocene as catalyst. Different alcohol to benzylamine ratios in the reaction mixtures were used to study the effects of different C/O and O/N ratios in the physical, chemical, electronics and electric properties of synthesized CNOs as well as the iron core. These ratios played an important role in the morphology, the amount of amorphous carbon of the samples, the N doping of CNOs, the electrical conductivity, the specific capacitance as well as the phase of the iron core of the synthesized samples. The iron cores consist of iron carbide nanoparticles and some of them have a thin layer of iron oxide on their surface. Due to the use of alcohol in the reaction mixtures, the synthesized CNOs presented oxygenated groups anchored on the CNOs surface, allowing their good dissolution in polar solvents. The synthesized sample with well-defined CNOs contained the biggest amount of amorphous carbon and its fabricated film showed the lowest electrical conductivity. On the other hand, the samples containing the smallest amount of amorphous carbon showed a morphology more similar to carbon nanosheets with embedded iron carbide nanoparticles and presented the best film electrical conductivities. In the best conductivity samples, the CNOs are connected between them with turbostratic graphite ribbons, which is similar to the CNOs obtained annealing carbon nanodiamonds in argon atmosphere. However, the most conductive film showed lower specific capacitance than the less conductive sample, indicating the importance of increasing the conductivity of the CNOs but without decreasing their effective surface area for their use in EDLCs.

Acknowledgments

The authors acknowledge M. Sc. Beatriz A. Rivera, M. Sc. Ana I. Peña, Dr. Gladis Labrada and Dr. Hector G. Silva-Pereyra for technical assistance as well as to LINAN at IPICyT for providing access to its facilities. This work was supported by CONACYT through grants No. CB-2015-01-256484 (R.L.S), Atención a problemas nacionales No. 789 (L.F.C.R) and for scholarships (E.T.M, J. A.M.T, and J.V.C.S).

References

[1] Ajayan PM, Iijima S. Capillarity-induced filling of carbon nanotubes. Nature 1993; 361(6410):333-4.

[2] Saito Y, Tomita M, Hayashi T. Lac2 encapsulated in graphite nano-particle. Jpn J Appl Phys 1993; 32(2 B):L280-2.

[3] Vardharajula S, Ali SZ, Tiwari PM, Eroğlu E, Vig K, Dennis VA, et al. Functionalized carbon nanotubes: Biomedical applications. Int J Nanomedicine 2012; 7:5361-74.

[4] Aguiló-Aguayo N, Maurizi L, Galmarini S, Ollivier-Beuzelin MG, Coullerez G, Bertran E, et al. Aqueous stabilisation of carbon-encapsulated superparamagnetic α-iron nanoparticles for biomedical applications. Dalton Trans 2014; 43(36):13764-75.

[5] Chaitoglou S, Sanaee MR, Bertran E. Arc-Discharge Synthesis of Iron Encapsulated in Carbon Nanoparticles for Biomedical Applications. J Nanomater 2014; 2014:1-8.

[6] Sanaee M, Chaitoglou S, Aguiló-Aguayo N, Bertran E. Size Control of Carbon Encapsulated Iron Nanoparticles by Arc Discharge Plasma Method. Appl Sci 2016; 7(26):1-15.

[7] Mutuma BK, Rodrigues R, Ranganathan K, Matsoso B, Wamwangi D, Hümmelgen IA, et al. Hollow carbon spheres and a hollow carbon sphere/polyvinylpyrrolidone composite as ammonia sensors. J Mater Chem A 2017; 5(6):2539-49.

[8] Kong J, Franklin NR, Zhou C, Chapline MG, Peng S, Cho K, et al. Nanotube molecular wires as sensors. Science 2000; 287(January):622-5.

[9] Iijima S. Direct observation of the tetrahedral bonding in graphitized carbon black by high resolution electron microscopy. J Cryst Growth 1980; 50(3):675-83.

[10] Ugarte D. Curling and closure of graphitic networks under electron-beam irradiation. Nature 1992; 359(6397):707-9.

[11] Mykhailiv O, Zubyk H, Plonska-Brzezinska ME. Carbon nano-onions: Unique carbon nanostructures with fascinating properties and their potential applications. Inorganica Chim Acta 2017; 468:49-66.

[12] Kuznetsov VL, Chuvilin AL, Butenko Y V., Mal'kov IY, Titov VM. Onion-like carbon from ultra-disperse diamond. Chem Phys Lett 1994; 222(4):343-8.

[13] Qiao Z, Li J, Zhao N, Shi C, Nash P. Graphitization and microstructure transformation of nanodiamond to onion-like carbon. Scr Mater 2006; 54(2):225-9.

[14] Xiao J, Ouyang G, Liu P, Wang CX, Yang GW. Reversible nanodiamond-carbon onion phase transformations. Nano Lett 2014; 14(6):3645-52.

[15] Cabioc'h T, Jaouen M, Thune E, Guérin P, Fayoux C, Denanot M. Carbon onions formation by high-dose carbon ion implantation into copper and silver. Surf Coatings Technol 2000; 128-129:43-50.

[16] Choucair M, Stride JA. The gram-scale synthesis of carbon onions. Carbon 2012; 50(3):1109-15.

[17] Hou H, Schaper AK, Weller F, Greiner A. Carbon nanotubes and spheres produced by modified ferrocene pyrolysis. Chem Mater 2002; 14(9):3990-4.

[18] Sawant SY, Somani RS, Panda AB, Bajaj HC. Formation and characterization of onions shaped carbon soot from plastic wastes. Mater Lett 2013; 94:132-5.

[19] Chen LS, Wang CJ. Synthesis of Carbon Onions with High Purity by Chemical Vapor Deposition. Adv Mater Res 2013; 641-642(3):43-6.

[20] Segura-Cardenas E, López-Sandoval R, Hernández-Arriaga D, Percino J, Chapela VM, Reyes-Reyes M. Oxygen to carbon atoms ratio effect on the size, morphology and purity of functionalized carbon nanoshells by using alcohol mixtures as carbon source. Carbon 2014; 76:292-300.

[21] Simon P, Gogotsi Y. Materials for electrochemical capacitors. Nat Mater 2008; 7(11):845-54.

[22] McDonough J, Gogotsi Y. Carbon Onions: Synthesis and Electrochemical Applications. Electrochem Soc Interface 2013; 22(3):61-6.

[23] Zeiger M, Jäckel N, Mochalin VN, Presser V. Review: carbon onions for electrochemical energy storage. J Mater Chem A 2016; 4(9):3172-96.

[24] Gu W, Yushin G. Review of nanostructured carbon materials for electrochemical capacitor applications: Advantages and limitations of activated carbon, carbide-derived carbon, zeolite-templated carbon, carbon aerogels, carbon nanotubes, onion-like carbon, and graphene. Wiley Interdiscip Rev Energy Environ 2014; 3(5):424-73.

[25] Georgakilas V, Guldi DM, Signorini R, Bozio R, Prato M. Organic Functionalization and Optical Properties of Carbon Onions. J Am Chem Soc 2003; 125(47):14268-9.

[26] Liu H, Ye T, Mao C. Fluorescent carbon nanoparticles derived from candle soot. Angew Chemie - Int Ed 2007; 46(34):6473-5.

[27] Yang S, Cao L, Luo PG, Lu F, Wang X, Wang H, et al. Carbon Dots for Optical Imaging in Vivo. J Am Chem Soc 2009; 131(32):11308-9.

[28] Czerw R, Terrones M, Charlier JC, Blase X, Foley B, Kamalakaran R, et al. Identification of Electron Donor States in N-Doped Carbon Nanotubes. Nano Lett 2001; 1(9):457-60.

[29] Carroll DL, Redlich P, Blase X, Charlier JC, Curran S, Ajayan PM, et al. Effects of nanodomain formation on the electronic structure of doped carbon nanotubes. Phys Rev Lett 1998; 81(11):2332-5.

[30] Navarro-Santos P, Ricardo-Chávez JL, Reyes-Reyes M, Rivera JL, López-Sandoval R. Tuning the electronic properties of armchair carbon nanoribbons by a selective boron doping. J Phys Condens Matter 2010; 22(50).

[31] Plonska-Brzezinska ME, Dubis AT, Lapinski A, Villalta-Cerdas A, Echegoyen L. Electrochemical properties of oxidized carbon nano-onions: DRIFTS-FTIR and raman spectroscopic analyses. ChemPhysChem 2011; 12(14):2659-68.

[32] Liu Y, Kim DY. Enhancement of Capacitance by Electrochemical Oxidation of Nanodiamond Derived Carbon Nano-Onions. Electrochim Acta 2014; 139:82-7.

[33] Gao Y, Zhou YS, Qian M, He XN, Redepenning J, Goodman P, et al. Chemical activation of carbon nano-onions for high-rate supercapacitor electrodes. Carbon 2013; 51(1):52-8.

[34] Zhang J, Zou H, Qing Q, Yang Y, Li Q, Liu Z, et al. Effect of chemical oxidation on the structure of single-walled carbon nanotubes. J Phys Chem B 2003; 107(16):3712-8.

[35] Lin Y, Zhu Y, Zhang B, Kim YA, Endo M, Su DS. Boron-doped onion-like carbon with enriched substitutional boron: the relationship between electronic properties and catalytic performance. J Mater Chem A 2015; 3(43):21805-14.

[36] Shu C, Lin Y, Zhang B, Abd Hamid SB, Su D. Mesoporous boron-doped onion-like carbon as long-life oxygen electrode for sodium–oxygen batteries. J Mater Chem A 2016; 4(17):6610-9.

[37] Chen S, Bi J, Zhao Y, Yang L, Zhang C, Ma Y, et al. Nitrogen-doped carbon nanocages as efficient metal-free electrocatalysts for oxygen reduction reaction. Adv Mater 2012; 24(41):5593-7.

[38] Kim SM, Heo YK, Bae KT, Oh YT, Lee MH, Lee SY. In situ formation of nitrogen-doped onion-like carbon as catalyst support for enhanced oxygen reduction activity and durability. Carbon 2016; 101:420-30.

[39] Wu G, Nelson M, Ma S, Meng H, Cui G, Shen PK. Synthesis of nitrogen-doped onion-like carbon and its use in carbon-based CoFe binary non-precious-metal catalysts for oxygen-reduction. Carbon 2011; 49(12):3972-82.

[40] Tuinstra F, Koenig JL. Raman Spectrum of Graphite. J Chem Phys 1970; 53(3):1126-30.

[41] Knight DS, White WB. Characterization of diamond films by Raman spectroscopy. J Mater Res 1989; 4(02):385-93.

[42] Caņçado LG, Takai K, Enoki T, Endo M, Kim YA, Mizusaki H, et al. General equation for the determination of the crystallite size la of nanographite by Raman spectroscopy. Appl Phys Lett 2006; 88(16):2-5.

[43] Sadezky A, Muckenhuber H, Grothe H, Niessner R, Poschl U. Raman microspectroscopy of soot and related carbonaceous materials: Spectral analysis and structural information. Carbon 2005; 43(8):1731-42.

[44] Seong HJ, Boehman AL. Evaluation of Raman parameters using visible Raman microscopy for soot oxidative reactivity. Energy and Fuels 2013; 27(3):1613-24.

[45] Bogdanov K, Fedorov A, Osipov V, Enoki T, Takai K, Hayashi T, et al. Annealing-induced structural changes of carbon onions: High-resolution transmission electron microscopy and Raman studies. Carbon 2014; 73:78-86.

[46] Zeiger M, Jäckel N, Weingarth D, Presser V. Vacuum or flowing argon: What is the best synthesis atmosphere for nanodiamond-derived carbon onions for supercapacitor electrodes? Carbon 2015; 94:507-517.

[47] de Faria DLA, Venâncio Silva S, de Oliveira MT. Raman microspectroscopy of some iron oxides and oxyhydroxides. J Raman Spectrosc 1997; 28(11):873-8.

[48] Reyes-Reyes M, Hernández-Arriaga D, López-Sandoval R. Carbon-coated hexagonal magnetite nanoflakes production by spray CVD of alcohols in mixture with water. Mater Res Express 2015; 1(4).

[49] Reyes-Reyes M, Vila-Nio JA, López-Sandoval R, Silva-Pereyra HG. Thermal stability of magnetite hexagonal nanoflakes coated with carbon layers. J Phys D Appl Phys 2016; 49(13).

[50] Park E, Zhang J, Thomson S, Ostrovski O, Howe R. Characterization of phases formed in the iron carbide process by X-ray diffraction, Mossbauer, X-ray photoelectron spectroscopy, and Raman spectroscopy analyses. Metall Mater Trans B Process Metall Mater Process Sci 2001; 32(5):839-45.

[51] Pradhan SK, Nayak BB, Mohapatra BK, Mishra BK. Micro Raman spectroscopy and electron probe microanalysis of graphite spherulites and flakes in cast iron. Metall Mater Trans A Phys Metall Mater Sci 2007; 38(10):2363-70.

[52] McDonough JK, Frolov AI, Presser V, Niu J, Miller CH, Ubieto T, et al. Influence of the structure of carbon onions on their electrochemical performance in supercapacitor electrodes. Carbon 2012; 50(9):3298-309.

[53] Portet C, Yushin G, Gogotsi Y. Electrochemical performance of carbon onions, nanodiamonds, carbon black and multiwalled nanotubes in electrical double layer capacitors. Carbon 2007; 45(13):2511-8.

[54] Lu Y, Yan Q, Han J, Cao B, Street J, Yu F. Fischer–Tropsch synthesis of olefin-rich liquid hydrocarbons from biomass-derived syngas over carbon-encapsulated iron carbide/iron nanoparticles catalyst. Fuel 2017; 193:369-84.

[55] Furlan A, Jansson U, Lu J, Hultman L, Magnuson M. Structure and bonding in amorphous iron carbide thin films. J Phys Condens Matter 2015; 27(4).

[56] Kumar NA, Nolan H, McEvoy N, Rezvani E, Doyle RL, Lyons MEG, et al. Plasma-assisted simultaneous reduction and nitrogen doping of graphene oxide nanosheets. J Mater Chem A 2013; 1(14):4431.

[57] Tseng W-S, Tseng C-Y, Kuo C-T. Effects of Gas Composition on Highly Efficient Surface Modification of Multi-Walled Carbon Nanotubes by Cation Treatment. Nanoscale Res Lett 2009; 4(3):234-9.

[58] Sun D, Yan X, Lang J, Xue Q. High performance supercapacitor electrode based on graphene paper via flame-induced reduction of graphene oxide paper. J Power Sources 2013; 222:52-8.

[59] Hu T, Sun X, Sun H, Xin G, Shao D, Liu C, et al. Rapid synthesis of nitrogen-doped graphene for a lithium ion battery anode with excellent rate performance and super-long cyclic stability. Phys Chem Chem Phys 2014; 16(3):1060-6.

[60] Arrigo R, Hävecker M, Schlögl R, Su DS. Dynamic surface rearrangement and thermal stability of nitrogen functional groups on carbon nanotubes. Chem Commun 2008; (40):4891.

[61] Kundu S, Nagaiah TC, Xia W, Wang Y, Dommele SV, Bitter JH, et al. Electrocatalytic Activity and Stability of Nitrogen-Containing Carbon Nanotubes in the Oxygen Reduction Reaction. J Phys Chem C 2009; 113:14302-10.

[62] Liu YL, Xu EY, Sun PC, Chen TH. N-doped porous carbon nanosheets with embedded iron carbide nanoparticles for oxygen reduction reaction in acidic media. Int J Hydrogen Energy 2015; 40(13):4531-9.

Sample	*D1*	*D3*	*D4*	*Dtot = D1+D3+D4*	*G*
EB-91	**Peak position**	**Peak position**	**Peak position**	**Dtot Area**	**Peak position**
	1341.6 cm^{-1}	1180 cm^{-1}	1510 cm^{-1}	176.3	1589.1 cm^{-1}
	FWHM	**FWHM**	**FWHM**	**D4/Dtot**	**FWHM**
	151.8 cm^{-1}	166 cm^{-1}	122.7 cm^{-1}	0.14	75.0 cm^{-1}
	Peak area	**Peak area**	**Peak area**		**Peak area**
	143.4	8.3	24.6		97.2
EB-41	**Peak position**	**Peak position**	**Peak position**	**Dtot area**	**Peak position**
	1351.1 cm^{-1}	1180 cm^{-1}	1510 cm^{-1}	193.0	1598.0 cm^{-1}
	FWHM	**FWHM**	**FWHM**	**D4/Dtot**	**FWHM**
	114.5 cm^{-1}	160 cm^{-1}	102.3 cm^{-1}	0.085	68.0 cm^{-1}
	Peak area	**Peak area**	**Peak area**		**Peak area**
	156.9	19.7	16.4		85.1
IB-91	**Peak position**	**Peak position**	**Peak position**	**Dtot area**	**Peak position**
	1354.9 cm^{-1}	1180 cm^{-1}	1510 cm^{-1}	205.3	1589.7 cm^{-1}
	FWHM	**FWHM**	**FWHM**	**D4/Dtot**	**FWHM**
	180 cm^{-1}	180 cm^{-1}	89.3 cm^{-1}	0.082	77.1 cm^{-1}
	Peak area	**Peak area**	**Peak area**		**Peak area**
	166.7	21.8	16.8		85.5
IB-41	**Peak position**	**Peak position**	**Peak position**	**Dtot area**	**Peak position**
	1366.4 cm^{-1}	1185 cm^{-1}	1510 cm^{-1}	154.8	1590.2 cm^{-1}
	FWHM	**FWHM**	**FWHM**	**D4/Dtot**	**FWHM**
	205.5 cm^{-1}	145.6 cm^{-1}	68.5 cm^{-1}	0.083	84.1 cm^{-1}
	Peak area	**Peak area**	**Peak area**		**Peak area**
	136.1	5.8	12.9		78.7

Table I. Main parameters of the Gaussian and Lorentzian curves obtained after fitting of Raman spectra.

Sample	I_{D1}/I_G	*Crystallite sizes using Eq. 2*	A_{D1}/A_G	A_{Dtot}/A_G	*Crystallite sizes using D1 in Eq. 3*	*Crystallite sizes using Dtot in Eq. 3*
EB-91	0.859	5.12 nm	1.475	1.81	11.26 nm	9.2 nm
EB-41	0.928	4.74 nm	1.843	2.27	9.01 nm	7.31 nm
IB-91	0.683	6.44 nm	1.951	2.40	8.51 nm	6.92 nm
IB-41	0.589	7.47 nm	1.728	1.97	9.61 nm	8.42 nm

Table II. Intensity and area ratios of the different samples as well as crystalline size L_a obtained using the Knight-White (Eq. 2) and Cançado (Eq. 3) equations.

Figures

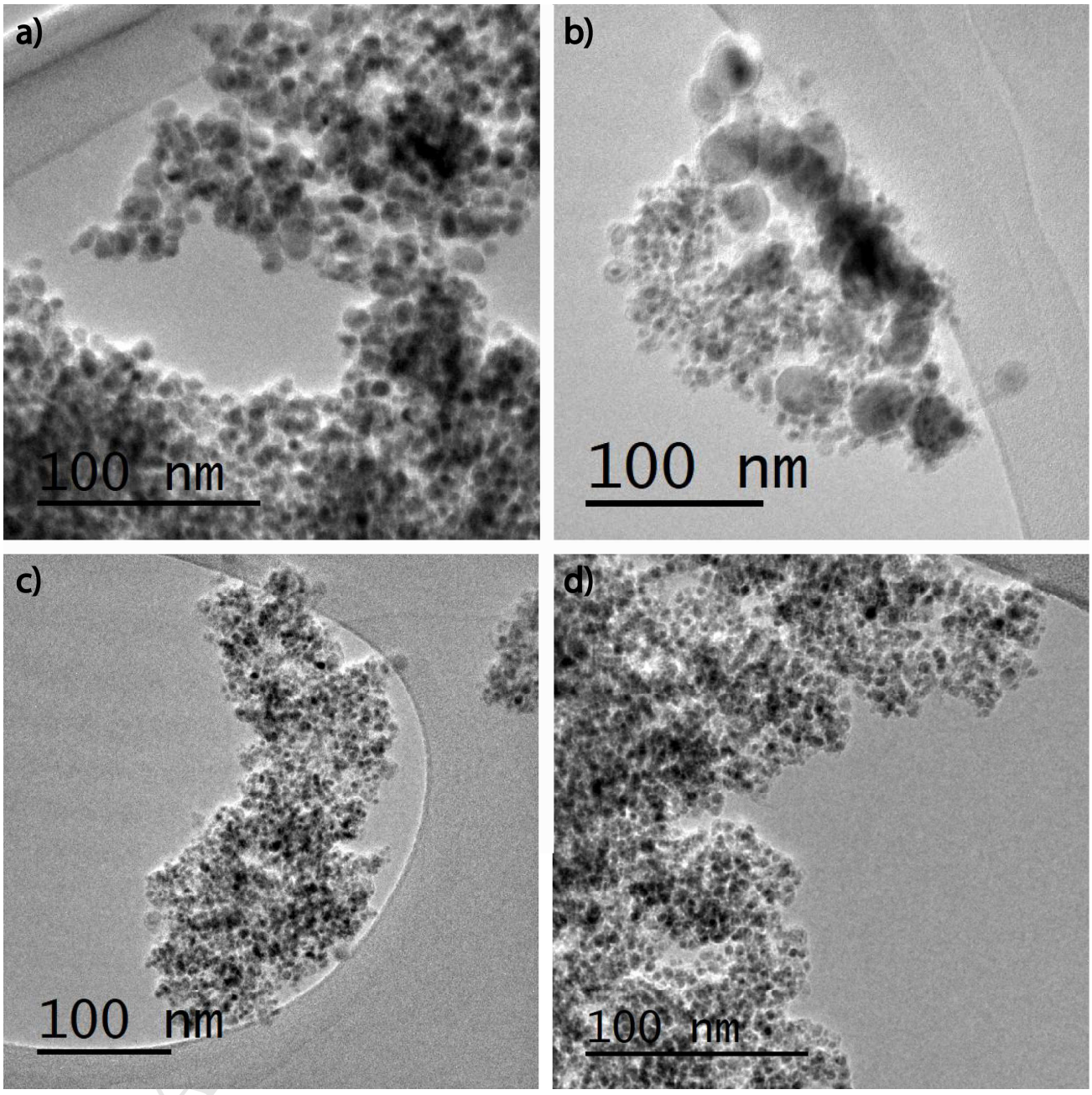

Figure 1. TEM micrographs of synthesized CNOs using the different alcohol-benzylamine reaction mixtures: (a) EB-91, (b) EB-41, (c) IB-91 and (d) IB-41.

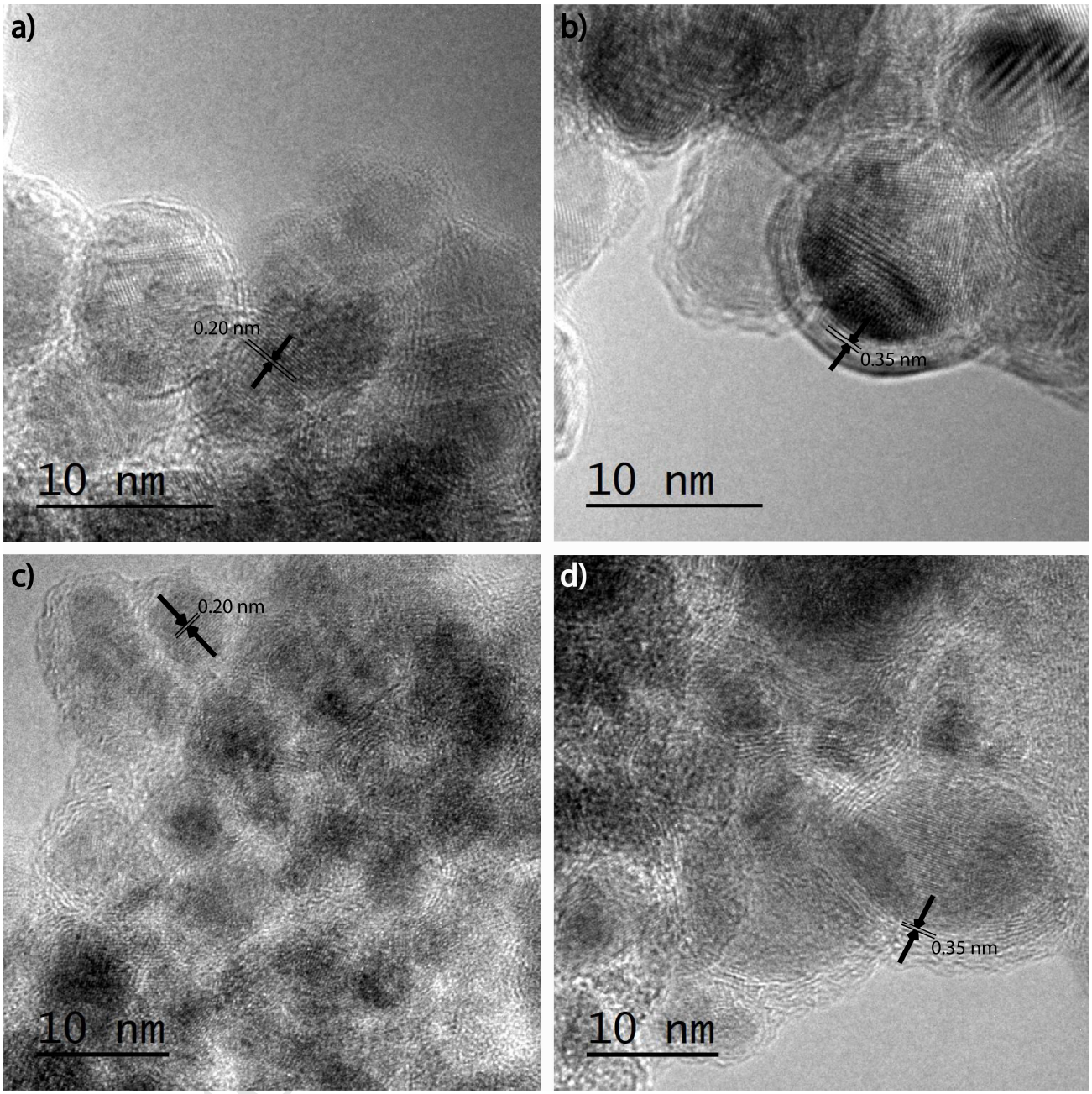

Figure 2. HRTEM micrographs of ethanol-benzylamine reaction mixtures at different v/v ratios: (a) and (b) EB-91 sample; it is observed a good graphitization of carbon shell encapsulating the iron carbide nanoparticles. c) and d) EB-41 sample, the carbon shells encapsulating the iron carbide core are less graphitized.

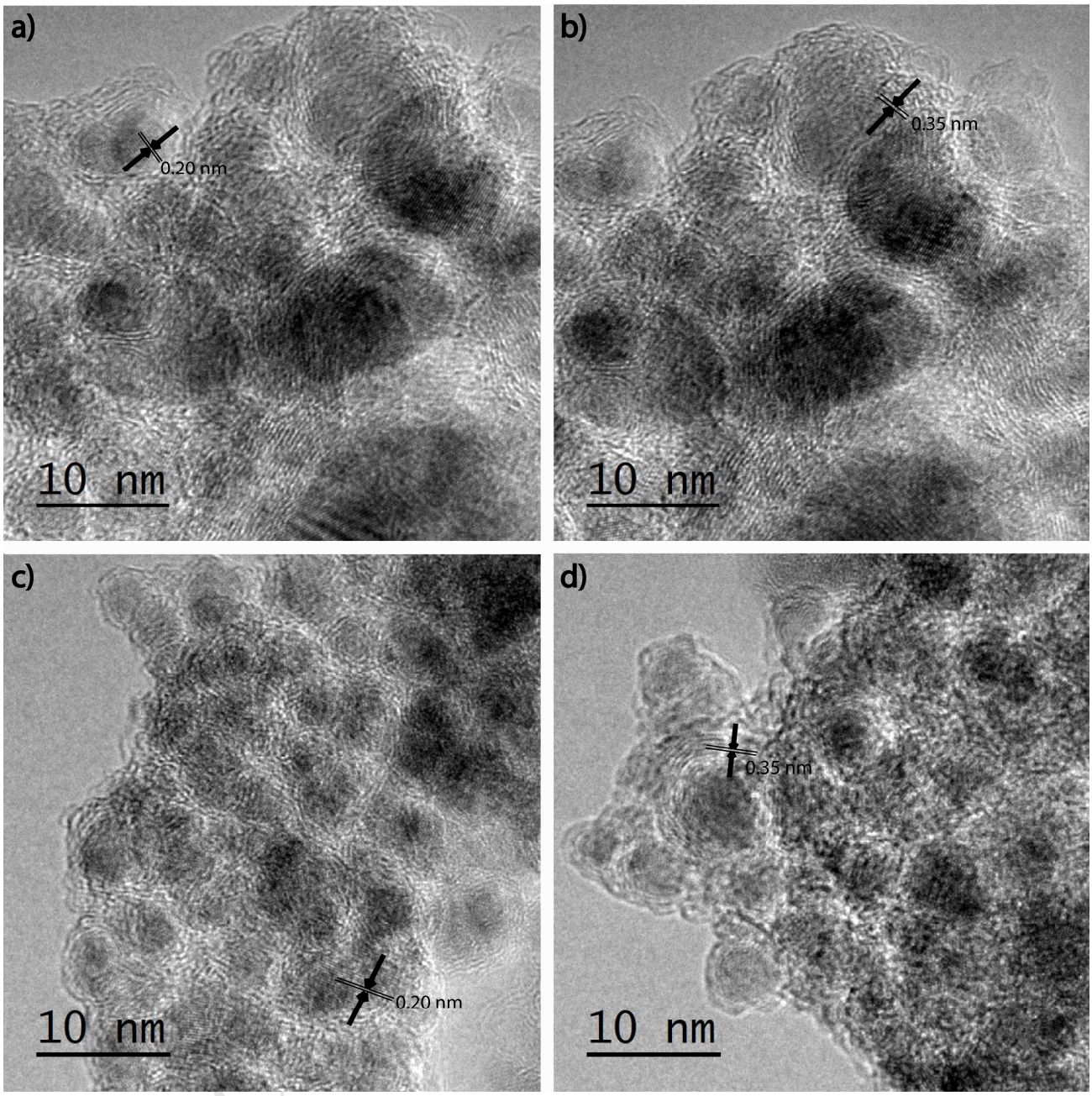

Figure 3. HRTEM micrographs of isopropanol-benzylamine reaction mixtures at different v/v ratios: (a) and (b) IB-91 sample. c) and d) IB-41 sample. In both cases the carbon shells encapsulating the iron core are not well graphitized.

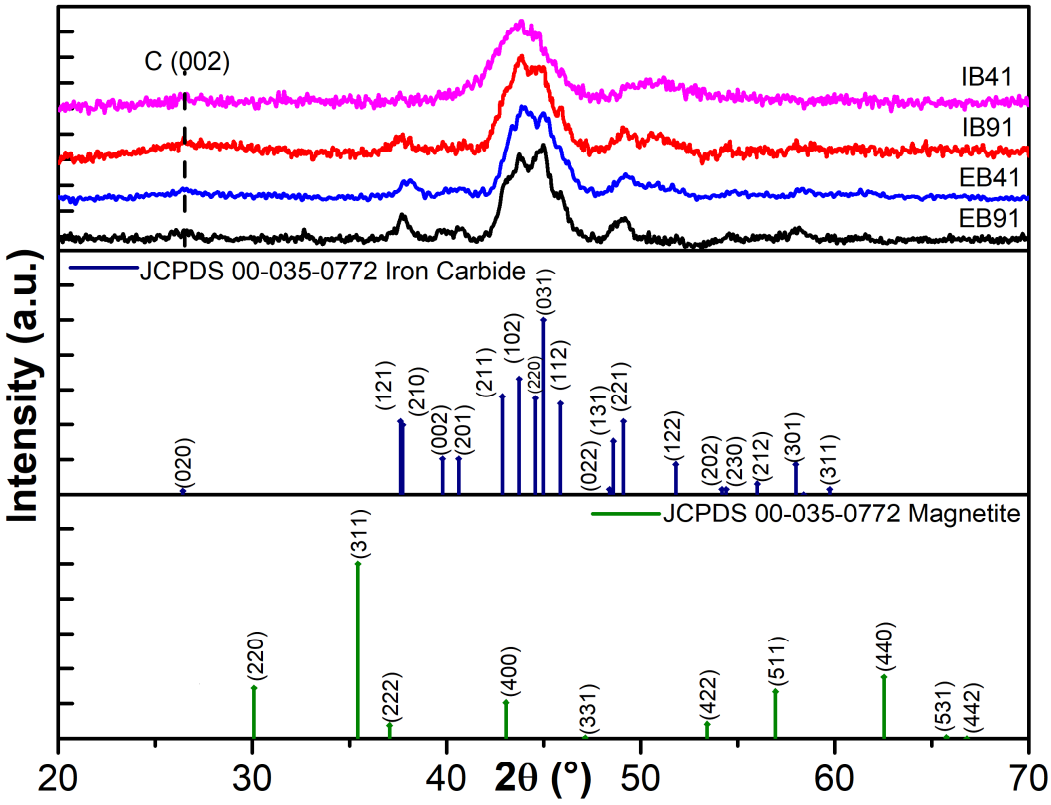

Figure 4. (Top) XRD diffraction patterns from the different synthesized samples. (Bottom) Iron carbide and magnetite crystallographic cards are shown.

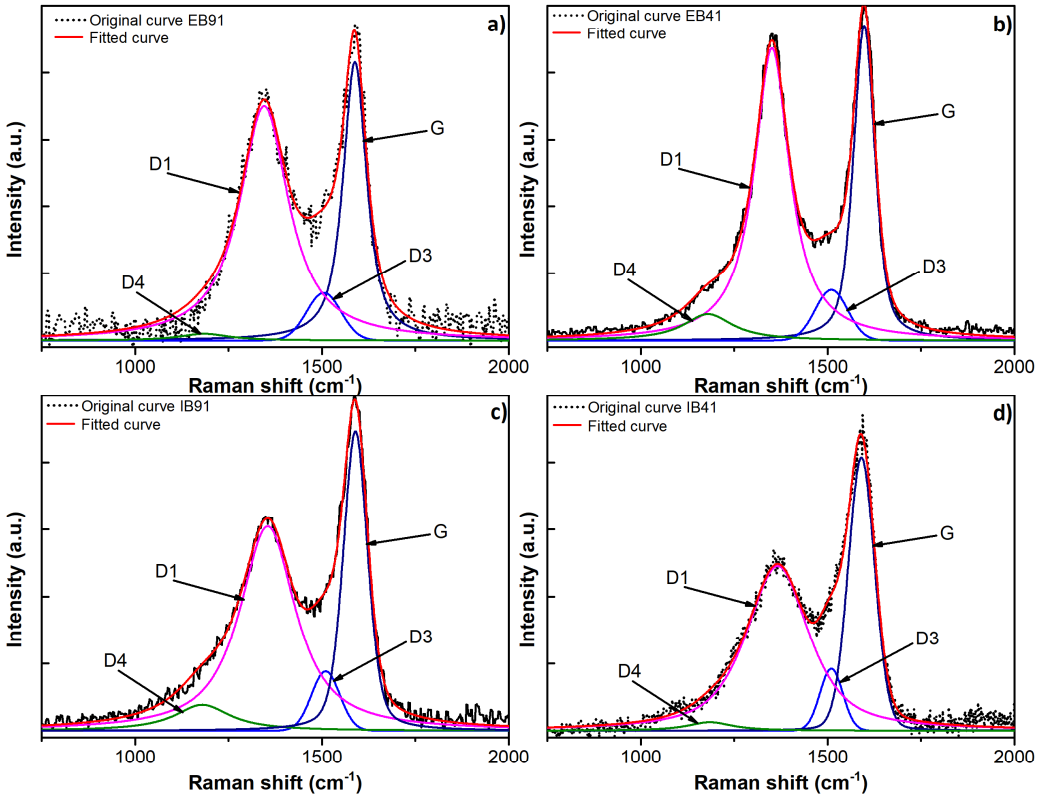

Figure 5. Raman spectra of synthesized samples and their fitted curves. Raman spectra were obtained using a 514 nm laser line with a power of 0.5 mW.

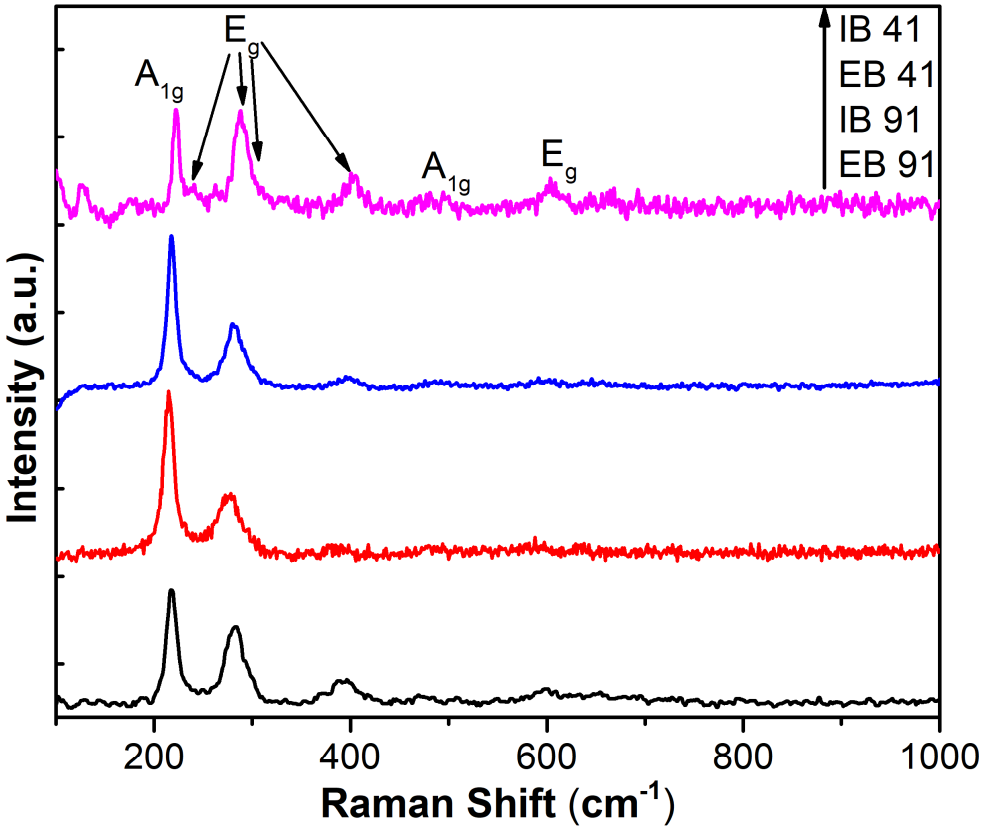

Figure 6. Raman spectra of the samples using a 2.5 mW laser power. The carbon shells encapsulating the iron core are eroded due to the laser power used during Raman characterization.

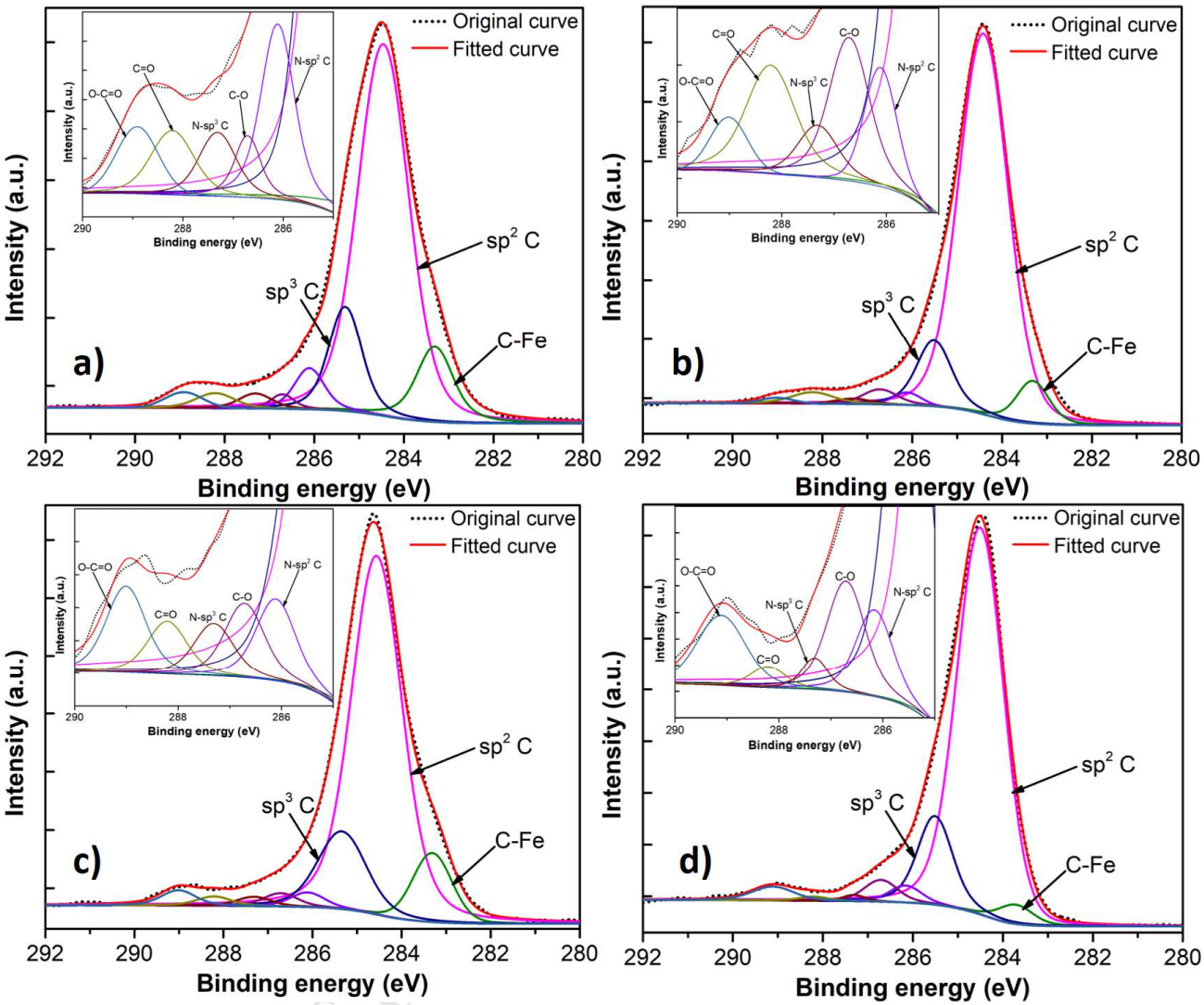

Figure 7. C1s XPS spectra with their respective deconvoluted peaks of the synthesized samples: (a) EB-91, (b) EB-41, (c) IB-91 and (d) IB-41.

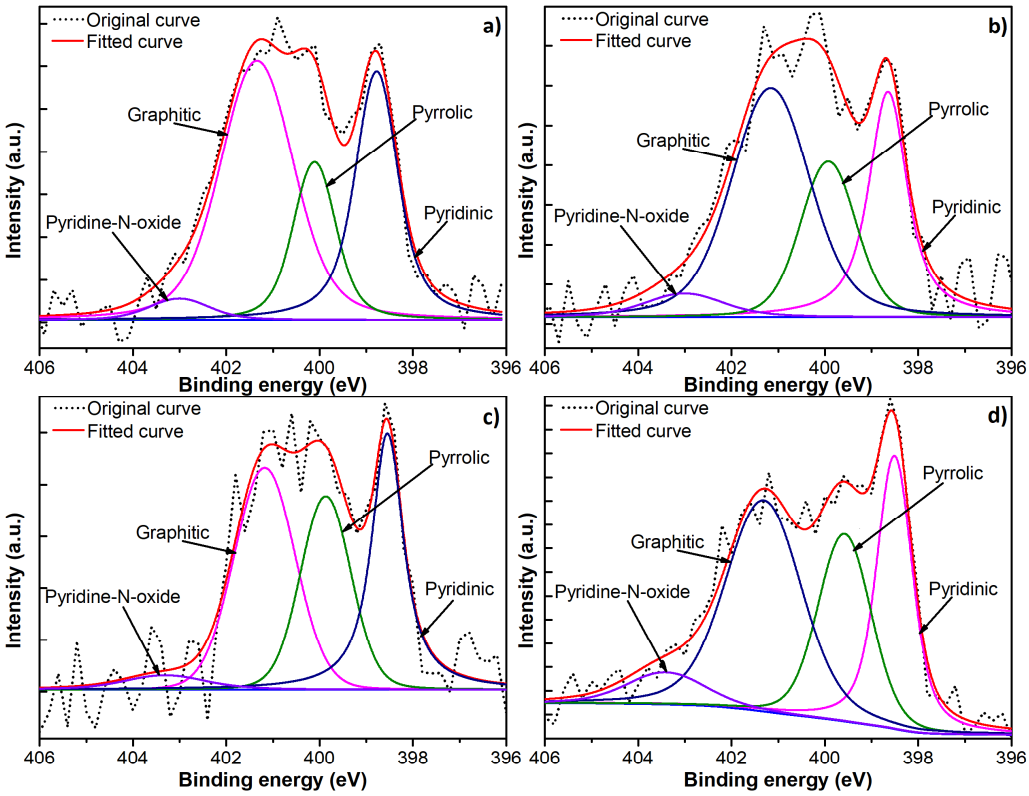

Figure 8. N1s XPS spectra with their respective deconvoluted peaks of the synthesized samples: (a) EB-91, (b) EB-41, (c) IB-91 and (d) IB-41.

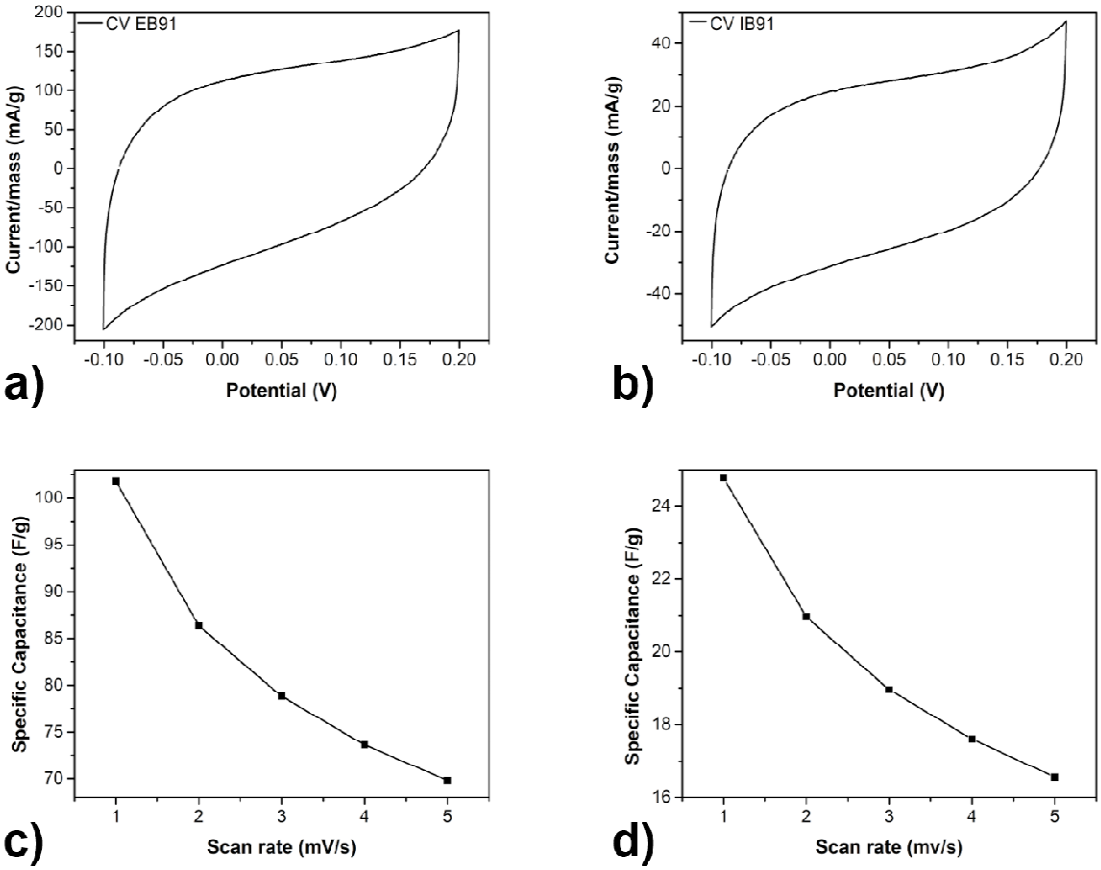

Figure 9. Cyclic Voltamograms of electrodes fabricated with (a) EB-91 and (b) IB-91 samples, in aqueous KOH 2 M at a scan rate of 1 mVs^{-1}. Specific capacitance of (c) EB-91 and (d) IB-91 electrodes at scan rates between 1 and 5 mV s^{-1}.